

# Modeling Hybrid Stars with an SU(3) Sigma Model

Rodrigo Nereiros\*

*FIAS, Goethe University, Ruth Moufang Str. 1 60438 Frankfurt am Main, Germany*

V.A. Dexheimer†

*Gettysburg College, Gettysburg, USA*

S. Schramm‡

*CSC, FIAS, ITP, Johann Wolfgang Goethe University, Frankfurt am Main, Germany*

(Dated: October 30, 2018)

We study the behavior of hybrid stars using an extended hadronic and quark SU(3) non-linear sigma model. The degrees of freedom change naturally, in this model, from hadrons to quarks as the density/temperature increases. At zero temperature, we reproduce massive neutron stars containing a core of hybrid matter of 2 km for the non-rotating case and 1.18 km and 0.87 km, in the equatorial and polar directions respectively, for stars rotating at the Kepler frequency (physical cases lie in between). The cooling of such stars is also analyzed.

PACS numbers: 26.60.Dd, 11.30.Rd, 21.65.Qr, 97.60.Jd

## I. INTRODUCTION

As the densest bodies in the universe, neutron stars are one of the best suited candidates to look for quark matter. Studying when and how the deconfinement from hadronic to quark matter occurs is crucial for the understanding and identification of such phenomena. Usual approaches for hybrid neutron stars consist of two different models with separate equations of state for hadronic and quark phases (see e.g. [1]), connected at the point for which the pressure of the quark phase exceeds that of the hadronic one. Within our approach we employ a single model for the hadronic and quark phases, avoiding the need for two separate equations of state. This approach, that presents a more natural transition from hadronic to quark matter, allows us to follow the spin evolution of a hybrid star with a single equation of state. In this paper we will investigate the structural changes that follows the stellar spin-down and the subsequent effects on the cooling of the object.

The SU(3) non-linear sigma model introduces baryons and quarks as flavor-SU(3) multiplets. Baryons and quarks obtain their masses through their coupling to the scalar fields of the theory (with an additional coupling to the Polyakov loop as discussed below) via spontaneous symmetry breaking. We include the quark degrees of freedom in the hadronic model in analogy to the PNJL model [2] by using an effective field that can be related to the QCD Polyakov loop, defined via  $\Phi = \frac{1}{3}\text{Tr}[\exp(i \int d\tau A_4)]$ , where  $A_4 = iA_0$  is the temporal component of the SU(3) gauge field. The effect of the field is to suppress quarks in the low density/temperature

regime and baryons at high densities and temperatures, respectively.

This paper is divided as follows: in section II we review the properties of the model used for the composition and equation of state; in section III we present our results which encompass the structure of rotating and spherically symmetric compact stars, and cooling effects; and in section IV our conclusions are presented.

## II. THE MODEL

The Lagrangian density for the sigma-type model, in mean field approximation, is given by

$$L = L_{Kin} + L_{Int} + L_{Self} + L_{SB} - U, \quad (1)$$

where besides the kinetic energy term for hadrons, quarks, and leptons, the terms

$$L_{Int} = - \sum_i \bar{\psi}_i [\gamma_0 (g_{i\omega}\omega + g_{i\phi}\phi + g_{i\rho}\tau_3\rho) + M_i^*] \psi_i, \quad (2)$$

$$\begin{aligned} L_{Self} = & -\frac{1}{2}(m_\omega^2\omega^2 + m_\rho^2\rho^2 + m_\phi^2\phi^2) \\ & + g_4 \left( \omega^4 + \frac{\phi^4}{4} + 3\omega^2\phi^2 + \frac{4\omega^3\phi}{\sqrt{2}} + \frac{2\omega\phi^3}{\sqrt{2}} \right) \\ & + k_0(\sigma^2 + \zeta^2 + \delta^2) + k_1(\sigma^2 + \zeta^2 + \delta^2)^2 \\ & + k_2 \left( \frac{\sigma^4}{2} + \frac{\delta^4}{2} + 3\sigma^2\delta^2 + \zeta^4 \right) + k_3(\sigma^2 - \delta^2)\zeta \\ & + k_4 \ln \frac{(\sigma^2 - \delta^2)\zeta}{\sigma_0^2\zeta_0}, \end{aligned} \quad (3)$$

$$L_{SB} = m_\pi^2 f_\pi \sigma + \left( \sqrt{2} m_k^2 f_k - \frac{1}{\sqrt{2}} m_\pi^2 f_\pi \right) \zeta, \quad (4)$$

represent the baryon (and quark) – meson interactions, meson self-interactions, and an explicit chiral symmetry breaking term that is responsible for producing the

\* negreiros@fias.uni-frankfurt.de

† vantoche@gettysburg.edu

‡ schramm@th.physik.uni-frankfurt.de

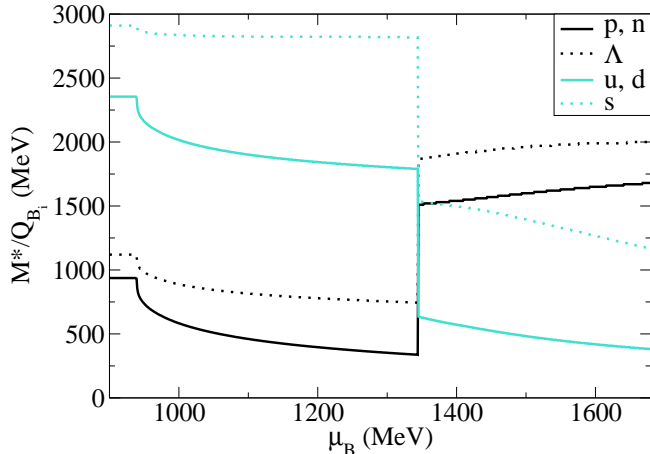


FIG. 1. (Color online) Effective normalized mass of different species as a function of baryonic chemical potential for star matter at zero temperature [3].

masses of the pseudo-scalar mesons. We will discuss the potential  $U$  further along this paper. The model has a  $SU(3)$  flavor symmetry, and the index  $i$  denotes the baryon octet and the three light quarks. In our calculations we take into account the following mesons: the vector-isoscalars  $\omega$  and  $\phi$ , the vector-isovector  $\rho$ , the scalar-isoscalars  $\sigma$  and  $\zeta$  (non-strange and strange quark-antiquark states, respectively), and the scalar-isovector  $\delta$ . The coupling constants of the model can be found in reference [3]. They were fitted to reproduce the vacuum masses of the baryons and mesons, nuclear saturation properties (density  $\rho_0 = 0.15 \text{ fm}^{-3}$ , binding energy per nucleon  $B/A = -16.00 \text{ MeV}$ , nucleon effective mass  $M_N^* = 0.67 M_N$ , compressibility  $K = 297.32 \text{ MeV}$ ), asymmetry energy ( $E_{sym} = 32.50 \text{ MeV}$ ), and reasonable values for the hyperon potentials ( $U_\Lambda = -28.00 \text{ MeV}$ ,  $U_\Sigma = 5.35 \text{ MeV}$ ,  $U_\Xi = -18.36 \text{ MeV}$ ). The vacuum expectation values of the scalar mesons are constrained by reproducing the pion and kaon decay constants. A detailed discussion of the purely hadronic part of the Lagrangian can be found in [4–6].

The effective masses of the baryons and quarks are given by

$$M_B^* = g_{B\sigma}\sigma + g_{B\delta}\tau_3\delta + g_{B\zeta}\zeta + M_{0B} + g_{B\Phi}\Phi^2, \quad (5)$$

$$M_q^* = g_{q\sigma}\sigma + g_{q\delta}\tau_3\delta + g_{q\zeta}\zeta + M_{0q} + g_{q\Phi}(1 - \Phi), \quad (6)$$

where  $M_0$  is equal to 150 MeV for nucleons, 354 MeV for hyperons, 5 MeV for up and down quarks and 150 MeV for strange quarks.

Equations (5) and (6) show that as the field  $\Phi$  increases (with the increase in density/temperature) baryons are suppressed, giving way to the quark phase, effectively modeling the QCD deconfinement phase transition. The

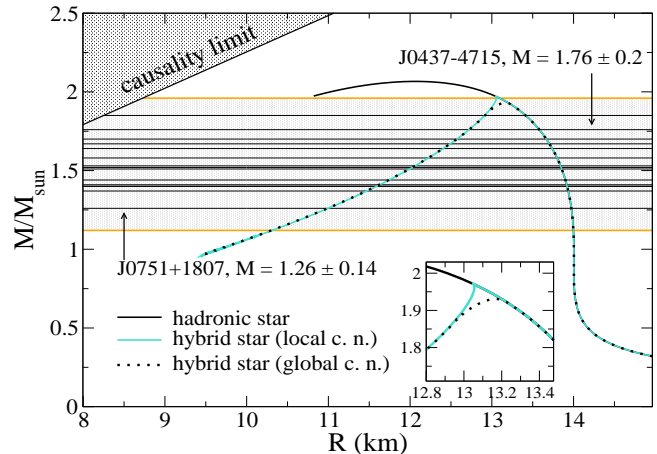


FIG. 2. (Color online) Mass-radius diagram for the model investigated in this paper. The horizontal lines represent observed pulsar masses ([9–15] and references therein). The band delimited by the two thick horizontal lines (orange lines online) represent the range of pulsars masses observed, accounting for the error of the highest and lowest observed mass.

opposite is true for low values of  $\Phi$  (at low density/temperature).

The effective normalized masses of baryons and quarks are shown in Fig. 1. Since the coupling constants in the  $\Phi$  term of the effective mass formulas are high but still finite, the effective masses of the species not present in each phase are large but also finite.

In analogy to the PNJL model, we define the potential  $U$  for  $\Phi$  as

$$U = (a_0 T^4 + a_1 \mu^4 + a_2 T^2 \mu^2) \Phi^2 + a_3 T_0^4 \log(1 - 6\Phi^2 + 8\Phi^3 - 3\Phi^4). \quad (7)$$

In our case,  $U(\Phi)$  is a simplified version of the potential used in [7, 8] and adapted to include terms that depend on the chemical potential. These two extra terms are not unique, but the most simple natural choice of extending the potential. The corresponding parameters are chosen to reproduce the main features of the phase diagram at finite densities. The coupling constants for the quarks can be found in reference [3], and are chosen to reproduce lattice data as well as known information about the phase diagram. The lattice data includes a first order phase transition at  $T = 270 \text{ MeV}$ , and a pressure function  $P(T)$  similar to refs [7, 8] at  $\mu = 0$  for pure gauge (for the quenched case without hadrons and quarks).

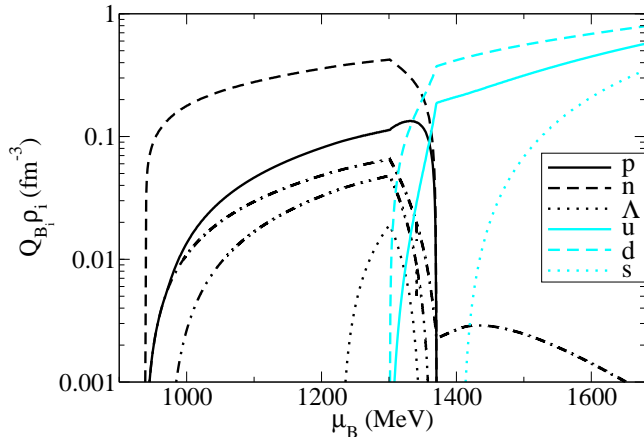


FIG. 3. (Color online) Population (baryonic density for different species as a function of baryonic chemical potential) for star matter at zero temperature using global charge neutrality [3].

### III. RESULTS

#### A. Deconfinement to Quark Matter

In our model the quarks are suppressed in the hadronic phase and the hadrons are suppressed in the quark phase, up to  $\mu_B = 1700$  MeV for  $T = 0$ . This behavior is due to the fact that the coupling constants in the  $\Phi$  term of the effective mass formulas are high but still finite, so in principle at very high chemical potential the threshold can be reached a second time for hadrons. This threshold, which is higher than the density in the center of neutron stars, establishes a limit for the applicability of the model. The hyperons, despite being included in the calculation, are suppressed by the appearance of the quark phase. Only a very small amount of Lambdas appears immediately before the phase transition. The strange quarks appear after the other quarks with relatively low abundance. The density of electrons and muons is significant in the hadronic phase but not in the quark phase, since the down and strange quarks are negatively charged, reducing the need for leptons to maintain charge neutrality.

Focusing on the high-density/low-temperature region of the phase diagram we are able to calculate neutron star masses and radii solving the Tolmann-Oppenheimer-Volkof equations [16, 17]. The solutions for hadronic (same model but without quarks) and hybrid stars are shown in Fig. 2, where besides our equation of state for the core, a separate equation of state was used for the crust [18]. The horizontal lines in Fig. 2 represent observed masses of some prominent millisecond pulsars ([9–15] and references therein). To avoid cluttering the graph we only indicated the name of the pulsars that establishes the lowest and highest observed masses: J0751+1807

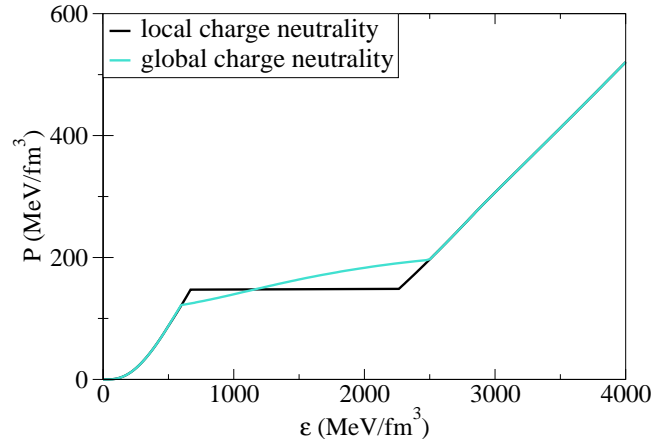


FIG. 4. (Color online) Equation of state (pressure as a function of energy density) for star matter at zero temperature using local and global charge neutrality [3].

with mass  $M/M_{\text{sun}} = 1.26 \pm 0.14$  [13] and J0437-4715 with  $M/M_{\text{sun}} = 1.76 \pm 0.2$  [9, 12] respectively. Any plausible equation of state must be able to produce neutron stars within the range delimited by these two objects, as is the case for the model investigated in this paper. Our model predicts a maximum neutron star mass of  $2.1 M_{\odot}$  considering local charge neutrality, which as shown in Fig. 2, is in agreement with the observational constraints shown. Comparing to the hadronic star sequence, the hybrid sequence has a much sharper peak. This peak (which denotes the most massive stable star in the sequence) signals the phase transition into quark matter at the core of the star. Because the equation of state for quark matter is much softer than the one for hadronic matter, the star becomes unstable at the point where the central density is higher than the phase transition threshold.

There is still another possible option for the configuration of the particles in the neutron star [19]. If instead of local we consider global charge neutrality, we find a mixture of phases even for zero temperature as discussed in [20]. This possibility, which is a more realistic approach, changes the particle densities in the coexistence region making them appear and vanish in a smoother way (Fig. 3). Therefore, the maximum mass allowed for the star is slightly lower in this case than in the previous one, as can be seen from the dotted line in Fig. 2; however, this possibility allows stable hybrid stars with a small amount of quarks. The mixed phase constitutes the inner core of the star up to a radius of approximately 2 km. The equation of state for both cases is shown in Fig. 4. The large jump in the pressure for the local charge neutrality case explains why the neutron stars become immediately unstable after the phase transition in this configuration.

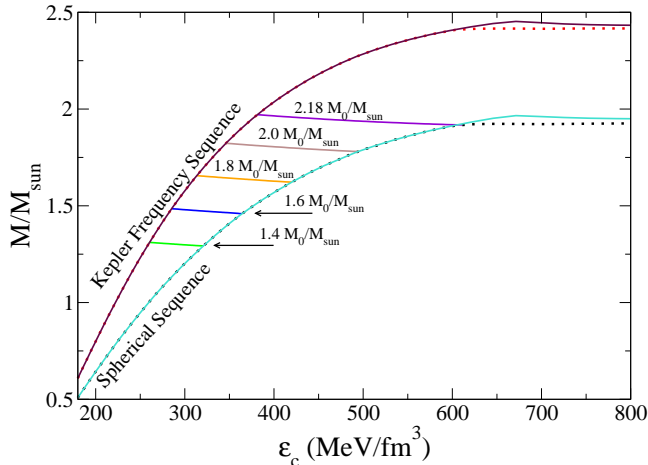


FIG. 5. (Color online) Gravitational mass as a function of central density. The lowermost sequences represent static stars ( $\Omega = 0$  Hz), whereas the higher most represents stars rotating at their Kepler frequency. The curves connecting the Kepler frequency to the static sequence are for stars with constant baryonic mass. These sequences represent the evolution of Kepler frequency stars to non-rotating objects.

### B. Rotational Effects

The results shown in Fig. 2 are for static neutron stars without including rotational effects. The rotational nature of pulsars (which in some cases may be rotating with frequencies as high as 700 Hz) warrants the investigation of the structure of rapidly rotating neutron stars, which is considerably more complicated than that of static objects. In References [6, 21] the rotational effects of the hadronic part of our model were investigated by means of the improved Hartle-Thorne perturbative method [22]. Here we will extend this research by performing exact rotational calculations and by including the quark-phase described in previous sections. The numerical method used for the solution of Einstein's field equations, and for the stellar structure of rapidly rotating neutron stars is based on the KEH method [23], which basically consists of expanding the metric functions in terms of Green's functions, which can be iteratively integrated, allowing us to calculate the structure of the star. This method has been expanded by several authors, and details can be found in References [24, 25].

In Fig. 5 we show the mass as a function of central density. The lowermost sequence represents static stars ( $\Omega = 0$  Hz), whereas the highest one represents stars rotating at their Kepler frequency. The Kepler frequency, or mass shedding frequency, is the maximum frequency at which a compact star may rotate. When rotating above this frequency an object would shed mass at its equator. This quantity therefore sets an absolute limit for the frequency of compact stars. The curves connecting

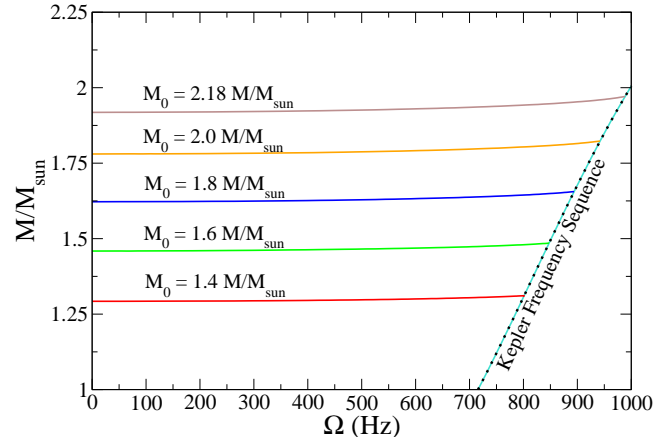


FIG. 6. (Color online) Gravitational mass as a function of frequency for the stars of Fig. 5. The stars from the static sequence are on the y-axis of the graph.

the Kepler frequency to the static sequence indicate stars with constant baryonic mass. These sequences represent the evolution of Kepler frequency stars to non-rotating objects. This is better illustrated in Fig. 6, which shows the gravitational mass as a function of frequency for the constant baryon mass stars. Fig. 6 also shows that the gravitational mass may be as high as 3% higher for a star rotating at the Kepler frequency (compared to a non-rotating star with same baryonic mass). The central density, on the other hand, may be decreased by as much as 38%, as shown in Fig. 5. It is important to stress that the constant baryon mass sequences shown in Figs. 5 and 6 represents the spin-down evolution of an isolated compact star (i.e. no accretion, hence the constant baryonic mass). Obviously the spin-down evolution is a function of time, therefore the x-axis of Figs. 6 could just as well be replaced by time. How the frequency (or equivalently the central density) varies with time will depend on the spin-down rate of the star. The computation of this quantity is not trivial, and depends on properties like magnetic field and/or gravitational radiation emission. Those issues are beyond the scope of the current paper, and therefore we show our results as a function of frequency and central density, always keeping in mind the implicit time dependence.

As shown in Figs. 5 and 6, when rotating at their Kepler frequency, neutron stars can attain higher masses. Loosely speaking this may be explained by the centrifugal force that provides an extra support against gravitational collapse. Even though we can find stable rotating neutron stars with masses up to  $\sim 2.5$  solar masses, these objects will collapse into black holes during spin-down evolution, which might be observable by the sudden stop of the neutrino signal originating from the star. As shown in Fig. 5, there is no stable static neutron star with baryon mass greater than 2.18 solar masses predicted by

our model.

The rotation also alters the redshift of the stars significantly. In Fig. 7 we show the forward redshift as a function of frequency for the stars of constant baryon mass of Fig. 5. As one can see, the forward redshift is substantially modified as the star's rotational frequency is reduced. In the extreme case of high frequencies the forward redshift becomes negative. For comparison purposes we have also plotted the redshift of the equivalent stellar sequences with no quark phase (purely hadronic matter). The redshift of these objects is almost identical to those of hybrid stars, with a very slight deviation for very high frequencies.

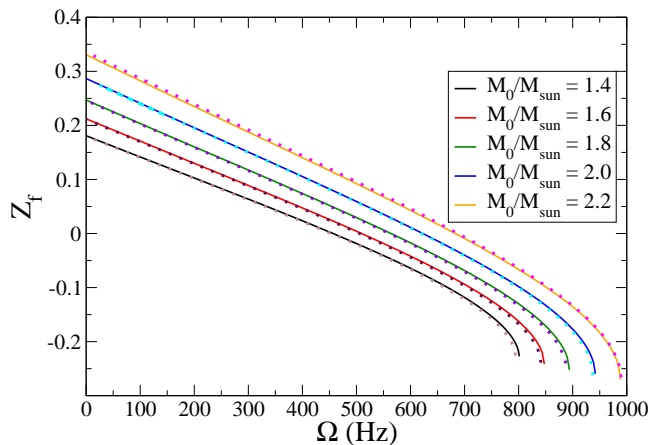


FIG. 7. (Color online) Forward redshift for the constant baryon mass sequences of Fig. 5. The dotted lines represent the redshift of the equivalent sequence for purely hadronic matter, which are almost identical to that of Hybrid stars.

Just as the redshift is changed during the spin-down evolution, the moment of inertia of the star should be modified as well. The moment of inertia as a function of frequency for the stars shown in Fig. 5 are given in Fig. 8.

Another particular feature of the model investigated here is the relatively low level of strangeness featured by the compact stars. As shown in Fig. 3 the  $\Lambda$  states (the first strange particle states to be populated) start to be occupied just before the onset of quark matter, which triggers the unstable branch of compact stars. Thus, the phase transition to quark matter suppresses the presence of strangeness in the object in the local charge neutrality case. Only for the densest objects we find a small region near the core with a low population of  $\Lambda$  states. The spin-down will also affect the strangeness of the object, increasing the radius of strangeness content near the core as the object spins down and becomes denser. This result is shown in Fig. 9 where the relative population ( $\rho_\Lambda/\rho_b$ ) for the  $\Lambda$  states is shown for frequencies of 988.4 Hz (a), 746.0 Hz (b), 356.3 Hz (c) and 0.0 Hz (d). This result represents the strangeness content of the

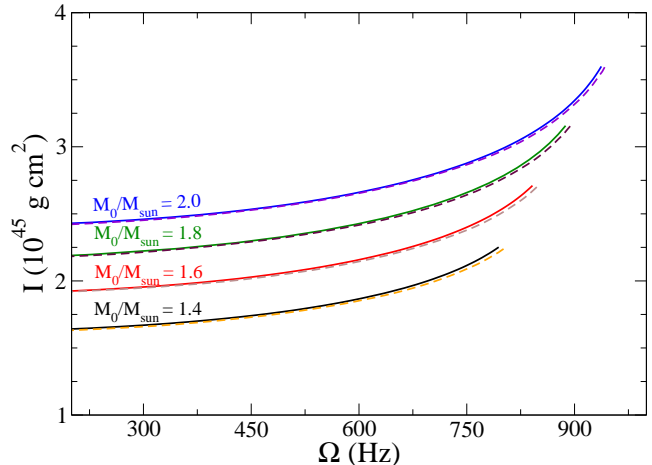


FIG. 8. (Color online) Moment of inertia for the constant Baryon mass sequences of Fig. 5. During the spin-down the geometry of the objects change significantly, and therefore the moment of inertia for these stars is substantially modified.

star, since no other particles containing strangeness are present. Fig. 9 shows that for higher frequencies (and thus lower densities) strangeness states are either absent, or are very lowly populated. As the object spins down, and its density increases, the strange core expands and becomes more highly populated. For comparison purposes in Fig. 10 we also show the strangeness content for a  $M_0/M_{\text{sun}} = 2.38$  stars in the pure hadronic model. In this case, since there is no phase transition to quark matter, the stars are able to attain higher masses (as can be seen in Fig. 2). Furthermore the hyperons are not suppressed by the onset of the quark phase, and these stars attain a higher strangeness content. As shown in Fig. 10, the  $\Lambda$  fraction at the core of the non-rotating star is 3.4 times higher than that found at the core of densest (stable) hybrid star. Once more we recall that the different frequencies shown in Figs. 9 and 10 represent different stages of time along the spin evolution of the star, with the time scale depending on the spin-down rate of the object.

### C. Cooling Process

Another method of probing the inner core of compact stars is by investigating its thermal evolution. All the thermal processes taking place in a compact star strongly depend on its composition, therefore by comparing theoretical predictions with observed thermal data, one can obtain valuable information regarding the core of neutron stars.

The thermal evolution of neutron stars is dominated by neutrino emissions for the first 1000 years (maybe more in the slow cooling scenario) [28], later being replaced

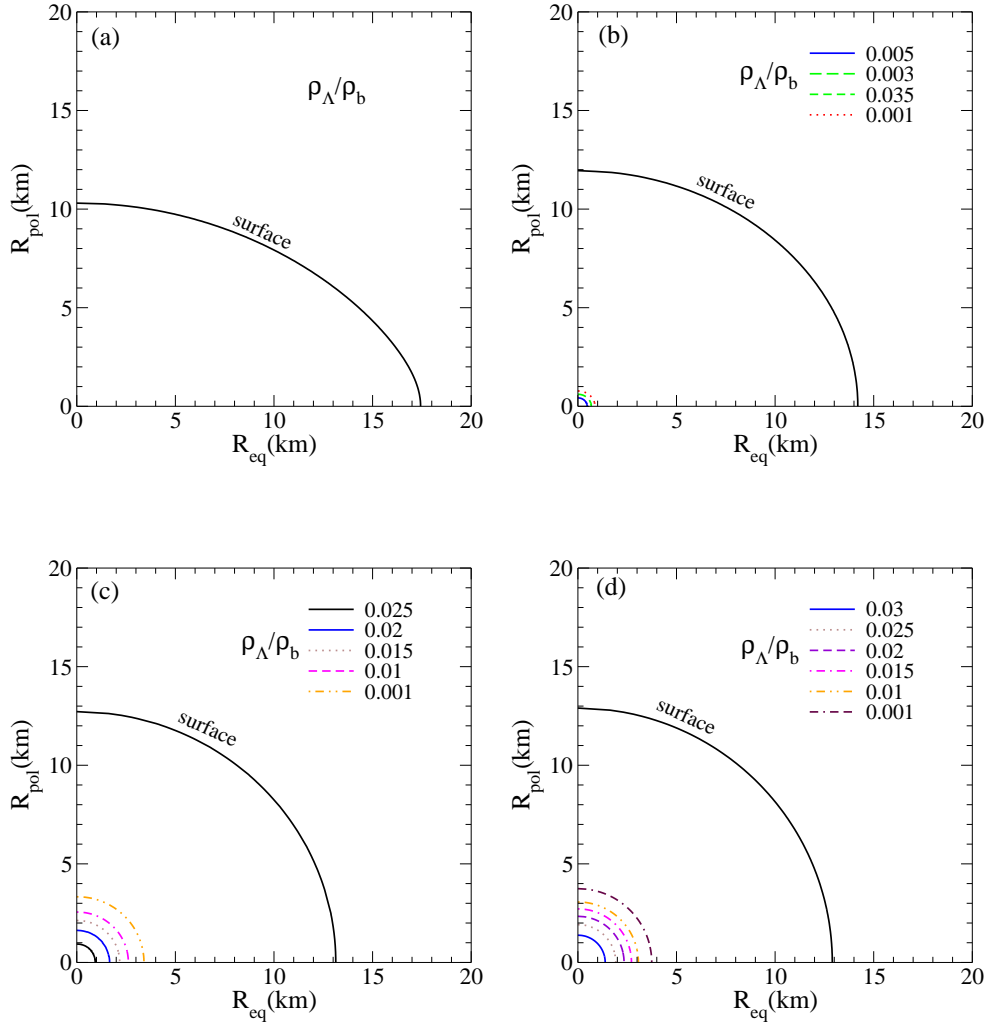


FIG. 9. (Color online) Strangeness content for a compact star with  $M_0/M_{\text{sun}} = 2.18$ , for frequencies of 988.4 Hz (a), 746.0 Hz (b), 356.3 Hz (c) and 0.0 Hz (d). The z axis represents the relative population of  $\Lambda$  ( $\rho_\Lambda/\rho_b$ ).

by photon emission from the surface. The direct Urca process [29] (DU process hereafter) is the most efficient cooling mechanism in a neutron star. With emissivities of the order of  $10^{26} \text{erg cm}^3 \text{s}^{-1}$  [29], neutron stars in which the DU process takes place will cool very quickly. Due to momentum conservation however, the DU process can only take place when the proton fraction reaches a certain value (which depends on the underlying equation of state, but it is usually between 11 – 15 %). Compact stars, whose proton fraction are below this threshold, will feature a slower cooling. Other processes, like pairing and meson condensates, for example, might have an influence on whether or not a neutron star will feature a fast or slow cooling. These topics are beyond the scope of the current research and will be pursued in future investigations.

We solve the thermal evolution equations [30] for the spherically symmetric stars shown in Fig. 2. The emission processes considered for the core are the direct Urca process [29], the modified Urca process [31], and the

Bremsstrahlung process [31, 32]; as for the crust we consider the electron Bremsstrahlung process [33], electron-positron annihilation [34] and plasmon decay [34]. The results are shown in Fig. 11, where we show the cooling curves for neutron stars with different gravitational masses. The symbol  $T_\infty$  denotes the redshifted temperature as detected by an observer at an infinite distance from the star.

We have also plotted some prominent observed temperatures of neutron stars [26, 27]. Since there are two estimates for the age of pulsars, we have plotted two sets of observed data. The first set is for objects whose age estimate is based on the observed spin down rate, these are represented by squares. The second set is for ages obtained by tracking the pulsar back to its original supernova remnant (kinematic age, represented by circles).

As shown in Fig. 11 our model is in relatively good agreement with the observed data, with the exception of a few high temperature pulsars. It is possible that

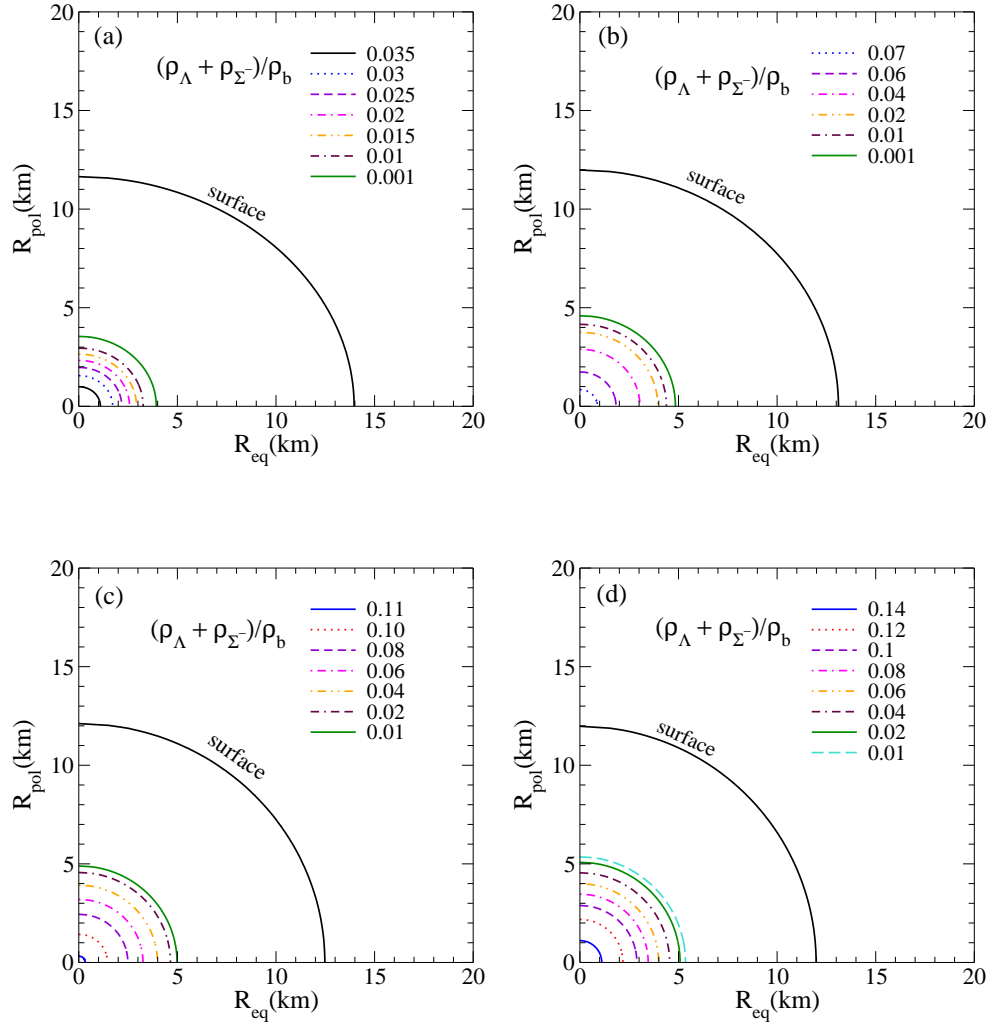


FIG. 10. (Color online) Strangeness content for a compact star with  $M_0/M_{\text{sun}} = 2.38$  in the pure hadronic model. The frequencies are 828.3 Hz (a), 639.9 Hz (b), 394.8 Hz (c) and 0.0 Hz (d). The z axis represents the relative population of  $\Lambda$  and  $\Sigma^-$  ( $(\rho_\Lambda + \rho_{\Sigma^-})/\rho_b$ ).

these objects feature non-standard processes like pairing or some re-heating mechanism which would explain their high temperature. The shaded area represents all possible cooling curves for our model, that can be obtained by solving the cooling equations for the whole spectrum of stable hybrid stars shown in Fig. 2. We can also see that within our model, neutron stars with masses higher than 1.22 solar masses, which feature an enhanced cooling, cool down too fast to be in agreement with observed data. It is important to mention that these results can be further improved if one consider more sophisticated processes like pairing and meson condensation.

Finally we have also investigated how spin down effects might affect the thermal evolution. As shown in Fig. 9, the increase in density that follows spin down has a strong effect on the strangeness content of the star. It is only natural to expect that other particle states will also be altered by the spin down. Particularly interesting

is the proton, electron and neutron populations, since these particle population will dictate whether or not the direct Urca process takes place. This process can only take place if the following triangle inequality (and cyclic permutations of it) is satisfied

$$k_n^f + k_p^f \geq k_e^f, \quad (8)$$

with  $k_i^f$  denoting the Fermi momentum of particle  $i$ . We calculated the radius threshold for different frequency stars, from the sequence with  $M_0/M_{\text{sun}} = 1.6$ . This result is shown in Fig. 12, where the gray shaded represents the region in which the DU process is allowed to take place.

The results of Fig. 12 show that the region in which the DU process takes place changes substantially during the evolution of the compact star. For the case studied, for higher frequencies (where the density is lower) the DU process can only take place in a very small region near

## IV. CONCLUSION

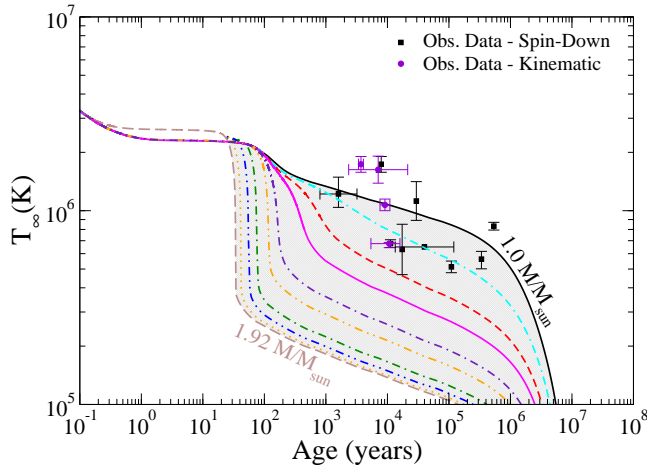


FIG. 11. (Color online) Cooling of a range of spherically symmetric neutron stars from Fig. 2. The symbol  $T_\infty$  denotes the redshifted temperature as detected by an observer at an infinite distance from the star. The onset of the direct Urca process happens for neutron stars with 1.22 solar masses. Any star with a lower mass will have a slow cooling. For masses above this value an enhanced cooling is achieved. Also shown is some prominent observed temperatures of neutron stars [26, 27]. Squares denote that the age was estimated based on the spin down rate, and circles indicate age estimates based on the motion of the pulsar with respect to its originating supernova remnant.

the core. This region grows as the stellar frequency decreases and the object becomes denser. This hints that the cooling of compact stars might be slower if one considers effects of spin down. Current efforts are in progress to better understand this issue, and will be discussed in a future paper.

Finally we have also generated a diagram  $\Omega(M)$  that shows the domain of frequencies and mass for which the direct Urca process is allowed. This result is shown in figure 13, where any star with mass and frequency that falls within the dark gray shaded area allows for the direct Urca process to take place. The light gray shaded area, on the top of the diagram, represents a forbidden region, where no stars can be found since their frequency would be above their Kepler frequency. The white area represents stars in which the direct Urca process cannot take place. Currently the spin of many X-ray burst sources is known, and in some cases their masses can also be inferred (see [35–37] and references therein). In the case of transient neutron stars, the core temperature can be inferred from the quiescent emission state [38]. Furthermore, for some neutron stars the spin frequency and the core temperature are bound (see for instance [39]). In the event that one might estimate the core temperature, spin frequency and stellar mass, the diagram shown in Fig. 13 might be used as a further test for this model.

A major advantage of our work, when compared to other studies of hybrid stars, is that because we have only one equation of state for different degrees of freedom we can study in detail the way in which chiral symmetry is restored and the way deconfinement occurs in the stars. Such phenomena happens, for example, during the star spin down.

We have found that SU(3) non-linear sigma model is suitable for the description of hybrid stars. The predicted maximum masses and the respective radii lie in the observed range. For a static object, our model predicts a star containing 2 km of hybrid matter (radius) surrounded by hadronic matter. In the event that the object is rotating at its Kepler frequency, the hybrid core becomes an oblate ellipsoid with equatorial and polar radii of 1.18 and 0.87 km, respectively. The reduction of the quark core for a rotating object should not be surprising, if one considers the reduction in density that follows rapid rotation.

We have also investigated the cooling of spherically symmetric (static) neutron stars, whose composition is described by our model. We have found that the threshold for the direct Urca process is reached for stars with mass greater than  $1.0 M_\odot$ . We have compared the cooling curves predicted by our model with some prominent observed compact stars temperature. We have found that, within our model, objects with masses up to  $1.22 M_\odot$  are in good agreement with the observed data. Any star with mass above this value features a thermal evolution that is too fast to be in agreement with the observed data. This result might seem inconsistent with the observed data, since most of these objects are expected to have a higher mass than  $1.22 M_\odot$ . It is important to notice that the results shown in Fig. 11 were obtained assuming a "froze-in" structure/composition. As noted in reference [38], many observed accreting neutron stars are in agreement with the slow cooling scenario. The fact that they are accreting implies that their structure is changing, as their frequency is modified as a result of the accretion process. As we showed in Fig. 12, the threshold radius for the direct Urca process strongly depends on the frequency of the star. Therefore, the fast cooling for stars with masses above  $1.22 M_\odot$  might be deceiving, since if we consider rotation we might obtain stars with  $M_0 = 1.6 M_\odot$  without presenting the direct Urca process (if the frequency is high enough). We could also see that a few observed objects present a very high temperature, that cannot be explained by our model. Most likely there is some non-trivial heating process taking place in these objects, which would explain why they are so warm at their relatively old ages, this topic however is beyond the scope of this work. It is important to mention that the quarks found in the 2 km hybrid core, have little effect on the cooling of these objects. Not only is the hybrid core very small, but the quarks are present at a smaller ratio than the hadrons, which allows the hadrons to dominate



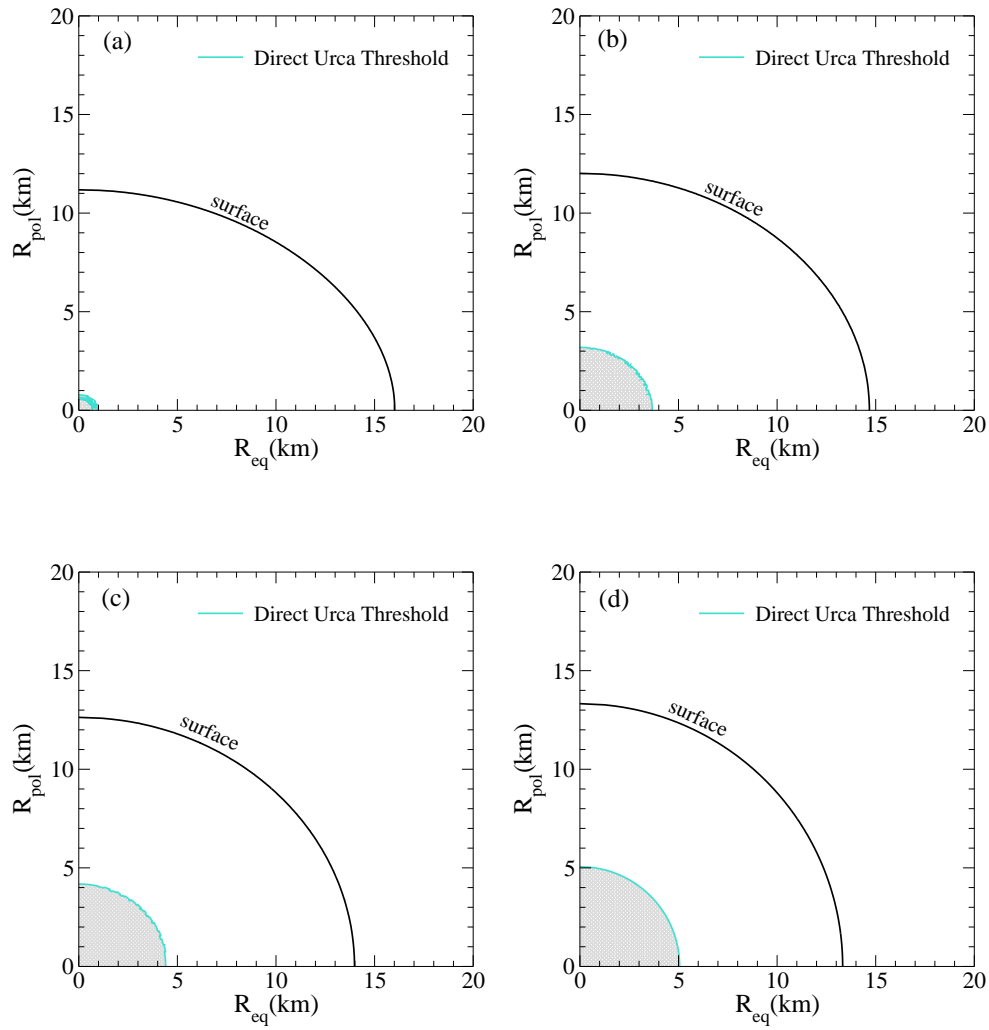


FIG. 12. (Color online) Direct Urca threshold for a compact star with  $M_0/M_{\text{sun}} = 1.6$ , for frequencies of 792.4 Hz (a), 656.8 Hz (b), 496.5 Hz (c) and 0.0 Hz (d). The grey shaded areas denotes the region in which the direct Urca process is allowed to take place (denoted by  $z=1$ ).

the cooling processes. On the other hand the suppression of hyperons, due to the onset of the quark phase is important. Since the hyperons do not appear in great quantities, some cooling channels (Hyperon Urca processes for instance) are not open. These channels are not very efficient cooling mechanisms [40], nonetheless their absence

slow down the cooling.

## V. ACKNOWLEDGEMENTS

We acknowledge the access to the computing facility of the Center of Scientific Computing at the Goethe-University Frankfurt for our numerical calculations.

- 
- [1] H. Heiselberg, C. Pethick, and E. Staubo, Physical Review Letters **70**, 1355 (1993).
  - [2] K. Fukushima, Physics Letters B **591**, 277 (2004).
  - [3] V. A. Dexheimer and S. Schramm, Physical Review C **81** (2010).
  - [4] P. Papazoglou, S. Schramm, J. Schaffner-Bielich, H. Stöcker, and W. Greiner, Physical Review C **57**, 2576

- (1998).
- [5] P. Papazoglou, D. Zschiesche, S. Schramm, J. Schaffner-Bielich, H. Stöcker, and W. Greiner, Physical Review C **59**, 411 (1999).
- [6] V. Dexheimer and S. Schramm, The Astrophysical Journal **683**, 943 (2008).

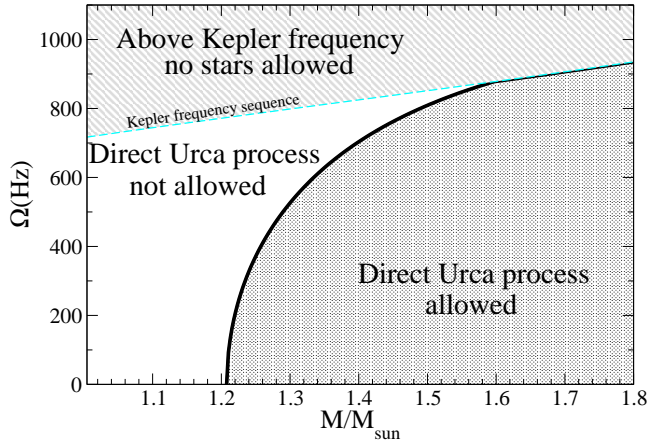


FIG. 13. (Color online)  $\Omega(M)$  diagram. Any star with mass and frequency that falls within the dark gray shaded area allows for the direct Urca process to take place. The light grey shaded area, on the top of the diagram, represents a forbidden region, where no stars can be found since their frequency would be above their Kepler frequency. Finally, the white area represents stars in which the direct Urca process cannot take place.

- [7] C. Ratti, M. Thaler, and W. Weise, *Physical Review D* **73**, 1 (2006).
- [8] S. Rößner, C. Ratti, and W. Weise, *Physical Review D* **75**, 1 (2007).
- [9] R. N. Manchester, G. B. Hobbs, A. Teoh, and M. Hobbs, *The Astronomical Journal* **129**, 1993 (2005).
- [10] I. H. Stairs, *Science (New York, N.Y.)* **304**, 547 (2004).
- [11] J. Lattimer and M. Prakash, *Physics Reports* **442**, 109 (2007).
- [12] J. P. W. Verbiest, M. Bailes, W. van Straten, G. B. Hobbs, R. T. Edwards, R. N. Manchester, N. D. R. Bhat, J. M. Sarkissian, B. A. Jacoby, and S. R. Kulkarni, *The Astrophysical Journal* **679**, 675 (2008).
- [13] P. C. C. Freire, A. Wolszczan, M. van Den Berg, and J. W. T. Hessels, *The Astrophysical Journal* **679**, 1433 (2008).
- [14] D. J. Champion, S. M. Ransom, P. Lazarus, F. Camilo, C. Bassa, V. M. Kaspi, D. J. Nice, P. C. C. Freire, I. H. Stairs, J. van Leeuwen, B. W. Stappers, J. M. Cordes, J. W. T. Hessels, D. R. Lorimer, Z. Arzoumanian, D. C. Backer, N. D. R. Bhat, S. Chatterjee, I. Cognard, J. S. Deneva, C.-A. Faucher-Giguère, B. M. Gaensler, J. Han, F. A. Jenet, L. Kasian, V. I. Kondratiev, M. Kramer, J. Lazio, M. A. McLaughlin, A. Venkataraman, and W. Vlemmings, *Science (New York, N.Y.)* **320**, 1309 (2008).
- [15] A. Kurkela, P. Romatschke, A. Vuorinen, and B. Wu, *Physical Review D* **4**(2010).
- [16] R. Tolman, *Physical Review* **55**, 364 (1939).
- [17] J. Oppenheimer and G. Volkoff, *Physical Review* **55**, 374 (1939).
- [18] G. Baym, C. Pethick, and P. Sutherland, *The Astrophysical Journal* **170**, 299 (1971).
- [19] N. Glendenning, *Physical Review D* **46**, 1274 (1992).
- [20] V. Dexheimer and S. Schramm, *Physical Review D* **3**(2009).
- [21] S. Schramm and D. Zschiesche, *Journal of Physics G: Nuclear and Particle Physics* **29**, 531 (2003).
- [22] N. Glendenning and F. Weber, *Physical Review D* **50**, 3836 (1994).
- [23] H. Komatsu, Y. Eriguchi, and I. Hachisu, *Royal Astronomical Society, Monthly Notices (ISSN 0035-8711)* **237** (1989).
- [24] G. B. Cook, S. L. Shapiro, and S. A. Teukolsky, *The Astrophysical Journal* **398**, 203 (1992).
- [25] N. Stergioulas and J. L. Friedman, *The Astrophysical Journal* **444**, 306 (1995).
- [26] D. Page, J. M. Lattimer, M. Prakash, and A. W. Steiner, *The Astrophysical Journal Supplement Series* **155**, 623 (2004).
- [27] D. Page, J. M. Lattimer, M. Prakash, and A. W. Steiner, *The Astrophysical Journal* **707**, 1131 (2009).
- [28] D. Page, U. Geppert, and F. Weber, *Nuclear Physics A* **777**, 497 (2006).
- [29] J. Lattimer, C. Pethick, M. Prakash, and P. Haensel, *Physical review letters* **66**, 27012704 (1991).
- [30] F. Weber, *Pulsars as astrophysical laboratories for nuclear and particle physics*, 1st ed. (Institute of Physics, Bristol, 1999).
- [31] B. Friman and O. Maxwell, *Astrophysical Journal* **232** (1979).
- [32] O. V. Maxwell, *The Astrophysical Journal* **231**, 201 (1979).
- [33] A. D. Kaminker, C. J. Pethick, A. Y. Potekhin, V. Thorsson, and D. G. Yakovlev, *Astronomy and Astrophysics* **343**, 1009 (1999).
- [34] D. Yakovlev, *Physics Reports* **354**, 1 (2001).
- [35] F. Özel, *Nature* **441**, 1115 (2006).
- [36] A. W. Steiner, J. M. Lattimer, and E. F. Brown, *Physical Review D* **50**(2010), astro-ph-HE/1005.0811.
- [37] V. Suleimanov, R. Poutanen, J. and K. Werner(2010), astro-ph-HE/1004.4871.
- [38] C. O. Heinke, P. G. Jonker, R. Wijnands, and R. E. Taam, *The Astrophysical Journal* **660**, 1424 (2007).
- [39] E. F. Brown, L. Bildsten, and P. Chang, *The Astrophysical Journal* **574**, 920 (2002).
- [40] M. Prakash, J. Lattimer, and C. Pethick, *Astrophysical Journal* **390**, L77 (1992).